This article has been accepted for publication in IEEE Transactions on Smart Grid. This is the author's version which has not been fully edited and content may change prior to final publication. Citation information: DOI 10.1109/TSG.2026.3715495

Distributed Resilient Control for Satellite-Aided Remote Microgrid Clusters

Zhijie Lian, *Member, IEEE*, Feiyang Liu, Huijie Yu, Yanyang Zhu, Yandong Chen, *Senior Member, IEEE*, Mohammad Shahidehpour, *Life Fellow, IEEE,* Quan Zhou, *Senior Member, IEEE*

***Abstract*— Integrated satellite-terrestrial networks (ISTNs) have emerged as a promising solution for the secure and stable operation of remote microgrid clusters. However, there exist inevitable measurement noise and satellite communication delay affecting the stability and coordinated control capabilities of remote microgrid clusters. To address the above challenges, this paper proposes an observer-based distributed resilient control strategy for satellite-aided remote microgrid clusters. First, a distributed observer is proposed to compensate for relative output estimation errors, based on which a distributed resilient secondary controller is designed to mitigate the impacts of noise and ISTN delays. Second, a guideline is presented for the controller parameter selection based on $\boldsymbol{H}_\infty$ performance. Third, it is theoretically proved that the system achieves voltage recovery and accurate current sharing considering noise and ISTN delays simultaneously with the proposed control strategy. Extensive case studies are conducted on an OPAL-RT real-time simulation platform equipped with a digital signal processor controller, where the proposed method can withstand a maximum noise level of $\boldsymbol{\sigma_s}$ =6 and a maximum delay of $\boldsymbol{\tau_D}$ =400 ms, demonstrating that it can effectively cope with the complex effects induced by strong noise and large delays under ISTNs.**

***Index Terms*—Distributed resilient control, remote microgrid clusters, satellite communication, ISTN delays.**

NOMENCLATURE

Variables

M, W, K_M, K^{total}, M_s, N_s, P, S, S_q, G_s, G_{si}	The number of satellites, ground stations (GS), microgrids within each GS coverage area, all microgrids in the network, subcarriers, consecutive symbols, propagation paths, respectively. The set of satellites, the qth satellite, the set of GS, the ith GS.
A, ψ, φ, H_0, R_S, v_s, θ, θ_0, d, d_{max}	Satellite positions, polar angle, azimuthal angle, radial distance, radius, velocity of the satellites, elevation angle of the qth satellite, minimal elevation angle of θ, distance between the qth satellite and the GS,
d_{min}, Φ, λ_s	maximum of d, minimum of d, homogeneous binomial point process, density of Φ.
Δf, T_s, f_c	Subcarrier spacing, symbol time duration, and carrier frequency.
$k_{p,q}$, $k_{max,q}$, f_D^{max}, $\alpha_{0,q}$	Doppler tap, maximum of Doppler tap, maximum of Doppler shift, the angle between the moving direction of the qth satellite to the GS.
V_N, V_i, $\bar{V}_i$, I_i, I_i^r, u_i,	Nominal voltage, output voltage, global average voltage, output current and rated current of the DGi, the secondary control input.
r_q, s_q, h_s, n_s, σ_s, L_q, L_{SF}, σ_{SF^2}, $h_{p,q}$	Doubly-selective faded signal, time-domain signal, total loss gain, the AWGN, the power spectral density of AWGN, path loss, shadowing fading loss, variance of L_{SF}, complex gain of the pth path of the qth S2G link.
T_Q, T_C, T_R, T_P, T_e, T_a, τ_D	Queueing delay, switching and processing delay, transmission delay, propagation delay, error-correction delay, the end-to-end total delay, the total delay.
u_i^W, u_i^F, e_i, e_i^{fd}, e_X, e_δ, e_n, T_m,	The distributed resilient control input, distributed fault estimation observer, combined error and dynamic error of the DGi, state estimation error, regulation error estimation error and noise estimation error, sampling time.
n_{si}, δ_i, $\hat{\delta}_i$, $\hat{n}_{si}$, ε_i	Noise of DGi, real regulation error of the DGi, estimated values of δ_i and n_{si}, relative output estimation error for the DGi.

Parameters

R_E, c	Radius of the Earth, velocity of light.
R_i^v, d_r, k_{Pi}, k_{Ii}, α_i, β_i, a_{ij}, g_i, k_{Wi}, k_{ei}, ρ_i, μ	Virtual impedance, design parameter for setting virtual impedance, proportional and integral control coefficients for the DGi. Error coefficients for the DGi, element values of the $\mathcal{A}$ and the G, controller gain and error gain within u_i^W, controller gain of u_i^F, tunable constant in the observer.

Matrices and Vectors

$\mathcal{A}$, $\mathcal{L}$, F, G	Adjacency matrix of the graph, Laplacian matrix of the graph, tunable parameter matrix, and loop-graph matrix.
H_1, H_2	Observer gain matrices.
$\mathbf{1}_N$	$N \times 1$ vector with all elements being 1.
I_N	N-dimensional identity matrix.

This work was supported in part by the General Project of National Natural Science Foundation of China under Grant 52477091, in part by the science and technology innovation Program of Hunan Province under Grant 2025RC3082, 2024RC1038. (Corresponding author: *Quan Zhou*).

Zhijie Lian, Feiyang Liu, Huijie Yu, Yanyang Zhu, Yandong Chen, Quan Zhou are with the College of Electrical and Information Engineering, Hunan University, Changsha 410082, China (e-mail: zquan@hnu.edu.cn).

Mohammad Shahidehpour is with the Electrical and Computer Engineering Department, Illinois Institute of Technology, Chicago, IL 60616 USA (e-mail: ms@iit.edu).

Authorized licensed use limited to: HUNAN UNIVERSITY. Downloaded on September 25,2026 at 04:45:13 UTC from IEEE Xplore. Restrictions apply.
© 2026 IEEE. All rights reserved, including rights for text and data mining and training of artificial intelligence and similar technologies. Personal use is permitted, but republication/redistribution requires IEEE permission. See https://www.ieee.org/publications/rights/index.html for more information.

This article has been accepted for publication in IEEE Transactions on Smart Grid. This is the author's version which has not been fully edited and content may change prior to final publication. Citation information: DOI 10.1109/TSG.2026.3715495

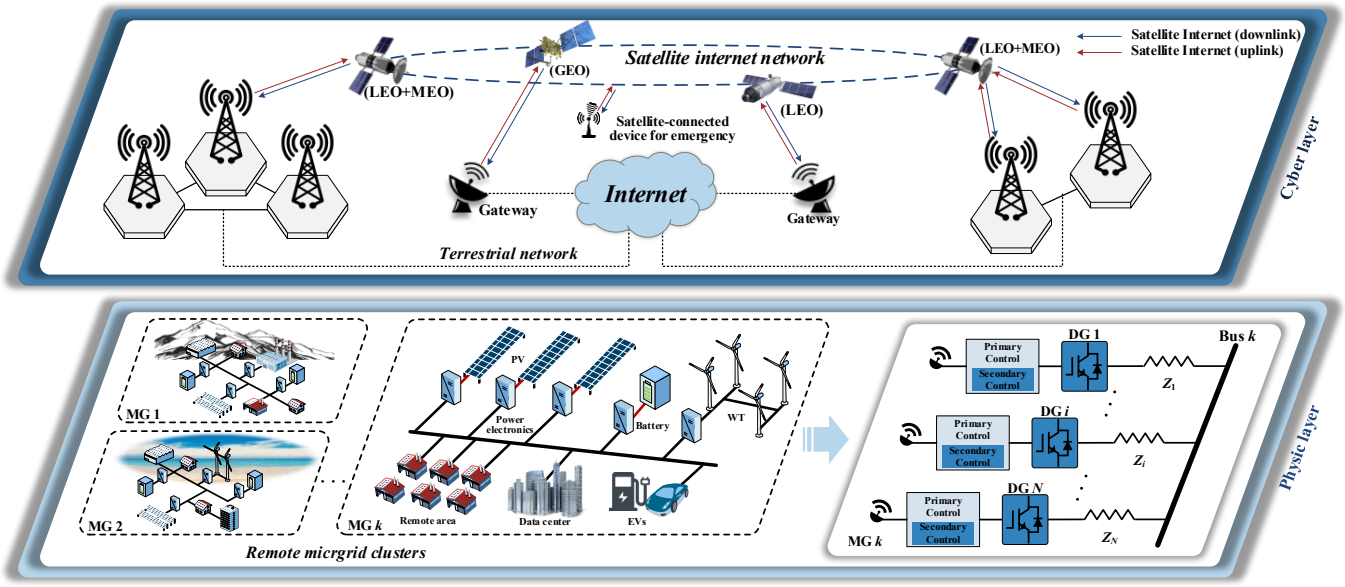


Fig. 1. Illustrative diagram of remote microgrid clusters under ISTNs.

I Introduction

Remote microgrid clusters consist of multiple interconnected microgrids, providing a reliable power supply and efficient energy utilization in remote regions through distributed generators (DGs), energy storage, and intelligent control [1]. Distributed control is a popular strategy to achieve accurate voltage restoration and current sharing, which relies on efficient and reliable communication systems to obtain transmission signals from neighboring microgrids [2]. However, existing terrestrial communication options are inadequate to meet the needs of remote microgrid clusters due to limitations in coverage, high installation costs, and susceptibility to environmental interference. Integrated satellite-terrestrial networks (ISTNs) have become a promising solution to overcome the above issues via integrating satellite communication with terrestrial networks, providing wide coverage, high reliability, and anti-interference communication support for remote microgrid clusters [3].

ISTNs leverage the advantages of satellite internet to provide global broadband access, supporting seamless network coverage for the effective management of renewable energy sources such as solar and wind power in distant regions, as shown in Fig. 1 [4]. For example, services like Starlink facilitate connectivity for remote renewable energy installations, including offshore wind farms and isolated solar arrays, ensuring the high integration and effective utilization of renewable energy resources in rural areas [5]. However, they still face numerous communication challenges when supporting the operation of remote microgrid clusters, particularly regarding noise and propagation delay. Compared to traditional terrestrial communication, ISTNs exhibit several unique characteristics. In terms of noise, satellite signals must traverse the atmosphere and are highly susceptible to weather conditions such as rain fade and cloud attenuation, resulting in pronounced non-stationarity in channel attenuation [6]-[7]. Additionally, Satellite-to-Ground (S2G) links are exposed to special interference sources, including solar radiation, cosmic background noise, and terrestrial electromagnetic interference, which further exacerbate the stochastic fluctuations in communication signals. In terms of delay, the inherent long propagation path of satellite communications leads to much higher delay compared to that of terrestrial networks. Typically, terrestrial communication delay ranges from 1 to 10 ms, whereas for low Earth orbit (LEO) satellite systems, where orbital altitudes range from 500 to 2000 km, the single-hop communication delay generally falls within the range of 10 to 30 ms [8]. More importantly, the satellite's orbital movement causes continuous variations in the satellite-ground distance, leading to dynamic changes in propagation delay. This dynamic delay is particularly pronounced during satellite handovers or link restoration after interruptions. Furthermore, the dynamic networking and inter-satellite link scheduling mechanisms adopted by LEO constellations introduce additional synchronization errors and queuing delays, further intensifying the uncertainty in communication delay.

In satellite-aided remote microgrid clusters, the practical implementation of centralized control is generally constrained by several factors, including a heavy communication burden, a high risk of single-point failure, limited scalability, and restricted computing capabilities [9]. Distributed control relies only on local information exchange among neighboring nodes, making it more suitable for the remote microgrid clusters considered in this paper [10]-[11]. Various control methods have been developed to address the noise issues in microgrid clusters [12]-[16]. In [12], a nonlinear generalized minimum variance control method was introduced into the secondary control system of islanded microgrids, effectively achieving noise attenuation, voltage/ frequency restoration, and reactive/active power sharing. In [13], a secondary control method for AC/DC hybrid inverters based on distributed anti-noise fixed-time consensus was proposed, where the system's convergence time is independent of initial conditions and can be precisely set offline according to regulatory requirements. Additionally, some researchers have studied a diffusion-based distributed Kalman filter, which integrates information from multiple nodes to achieve effective noise reduction and denoising [14]. To overcome the convergence obstruction

Authorized licensed use limited to: HUNAN UNIVERSITY. Downloaded on September 25,2026 at 04:45:13 UTC from IEEE Xplore. Restrictions apply.
© 2026 IEEE. All rights reserved, including rights for text and data mining and training of artificial intelligence and similar technologies. Personal use is permitted, but republication/redistribution requires IEEE permission. See https://www.ieee.org/publications/rights/index.html for more information.

This article has been accepted for publication in IEEE Transactions on Smart Grid. This is the author's version which has not been fully edited and content may change prior to final publication. Citation information: DOI 10.1109/TSG.2026.3715495

TABLE I
COMPARISON OF EXISTING DISTRIBUTED RESILIENT CONTROL METHODS FOR MICROGRIDS

Method	Focus	Noise Suppression	Overcoming Delays
Resilient distributed consensus protocol [13] [15]	Consensus under measurement noise	√	×
Diffusion-based distributed Kalman filter [14]	Noise reduction via multi-node fusion	√	×
Distributed predictive control [18]	Voltage tracking with delay/packet loss	×	√
Delay-tolerant control [20]	Resilience under random delays	×	√
Event-triggered control [21]	Resource optimization with delays	×	√
The proposed control	Resilient control for satellite-aided clusters	√	√

caused by nondecaying noise, a time-varying control gain mechanism is proposed, which ensures asymptotic unbiased consensus while sustaining long-term differential privacy preservation [15]. In addition to noise, the issue of propagation delays is also an inescapable issue affecting microgrid stability, which is not considered in the above methods [12]-[16].

In addition to noise interference, the long round-trip time of inter-satellite signal transmission and frequent link switching further increase communication latency, thereby weakening the coordinated control capability and dynamic response speed of the remote microgrid clusters. Existing related research mainly focuses on communication efficiency optimization, delay compensation, and robustness enhancement [17]-[22]. To address the voltage tracking problem, a consensus-based proportional-integral predictive control strategy has been proposed, considering communication delays and packet loss [18]. In [19], a resilient distributed multiagent control scheme is proposed for AC microgrids with additive noise and time-delay disturbances, achieving voltage, frequency, and power sharing. Beyond delay compensation, delay-tolerant control methods have been introduced to enhance the resilience of microgrids under random delays and variable sampling rates [20]. A hybrid dynamic event-triggering mechanism has been proposed to mitigate time-varying communication delays while ensuring that the event-triggering interval remains strictly positive, thereby optimizing communication resource utilization [21].

To better illustrate the differences and connections among these research contents, Table I is presented. It can be observed that existing distributed resilient control methods mostly focus on a single communication impairment: they address either noise or delays alone. In contrast, the observer-based distributed resilient control method proposed in this paper simultaneously tackles both noise and ISTN delays in satellite-aided microgrid clusters, achieving more comprehensive communication-resilient control.

Due to the uncertainty of the space environment and the inherent characteristics of ISTNs, remote microgrid clusters under ISTNs often face the dual challenges of noise and ISTN delays. To address these issues simultaneously and enhance the stability and coordination capability of microgrids under complex communication conditions, this paper proposes an observer-based distributed resilient control strategy. The main contributions are as follows:

1) A unified mathematical model of noise and ISTN delays in ISTN environments is established, revealing the key characteristics that distinguish ISTNs from traditional terrestrial communication. This model provides a theoretical foundation for developing an integrated distributed control framework to simultaneously address noise and delay issues in ISTNs.

2) Considering that noise is uncontrollable and cannot be eliminated, a distributed observer with tunable parameters is further proposed, which effectively leverages current output information to enhance the accuracy of noise estimation.

3) To enhance system robustness, a multi-constrained H_∞ observer design method based on pole placement is employed to calculate the observer gain, resulting in a reduced H_∞ performance index. Moreover, the effectiveness and feasibility of the proposed distributed resilient controller are validated through both theoretical analysis and experimental verification.

The remainder of this paper is organized as follows. In Section II, we present the physical and cyber models of microgrid clusters under ISTNs. In Section III, a distributed resilient secondary controller is designed, and its corresponding stability is analyzed. Section IV presents OPAL-RT experimental results to validate the effectiveness of the proposed method, and this paper is concluded in Section V.

II MODELING OF MICROGRID CLUSTERS UNDER ISTNS

This section introduces the ISTNs model, encompassing the network model, ground stations, and communication links, as well as the microgrid clusters model and its conventional secondary control. It elaborates on the space and ground segments of the ISTNs and the control strategies for each DG of the microgrid. Furthermore, it analyzes the impact of ISTNs on remote microgrid clusters.

A. ISTNs Model

In Fig. 2, the ISTNs model consists primarily of two interconnected parts, i.e., the space and ground segments. Inspired by [23]-[24], this paper will conduct modeling.

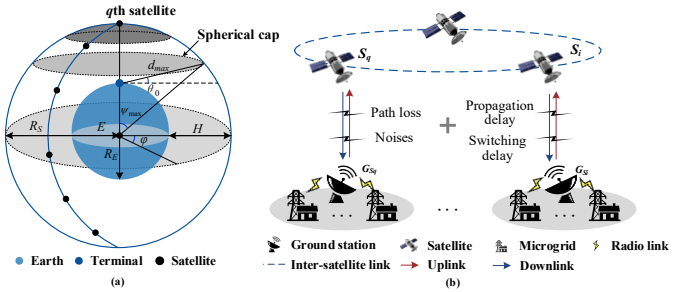


Fig. 2. Modeling of ISTNs. (a) Satellite orbit model. (b) Example of the network architecture model.

Authorized licensed use limited to: HUNAN UNIVERSITY. Downloaded on September 25,2026 at 04:45:13 UTC from IEEE Xplore. Restrictions apply.
© 2026 IEEE. All rights reserved, including rights for text and data mining and training of artificial intelligence and similar technologies. Personal use is permitted, but republication/redistribution requires IEEE permission. See https://www.ieee.org/publications/rights/index.html for more information.

This article has been accepted for publication in IEEE Transactions on Smart Grid. This is the author's version which has not been fully edited and content may change prior to final publication. Citation information: DOI 10.1109/TSG.2026.3715495

1) Network Model

We define that there are M satellites in the space segment, and let $S = \{S_1, \ldots, S_M\}$ represent the set of satellites, where S_q indicates the qth satellite. For the satellite communication system, we consider a scenario with all satellites at altitude H_0, communicating with terminals located on the Earth's surface with velocity v_s. M satellites are uniformly distributed on the surface of a sphere with the radius $R_E + H_0$, following a homogeneous binomial point process Φ with density λ_s, where R_E is the radius of the Earth. The satellite positions on the spherical surface are expressed with spherical coordinates as $\mathrm{A} = \{R_S = R_E + H_0, 0 \le \psi \le \pi, 0 \le \varphi \le 2\pi\}$, where H_0 is the radial distance, ψ is the polar angle, and φ is the azimuthal angle, respectively.

The distance between the qth satellite and the ground station (GS), which is assumed to be right under the orbit, can be determined by

$$d = \sqrt{R_E^2 \sin^2\theta + H_0^2 + 2R_E H_0} - R_E \sin\theta, \tag{1}$$

where θ is the elevation angle of the qth satellite, satisfying $\theta_0 \leqslant \theta \leqslant 90°$, where θ_0 is the minimal elevation angle of the connected range. As a result, in the connected range where $\theta \ge \theta_0$, the distance d satisfies $d_{\min} \le d \le d_{\max}$, where $d_{\max} = \sqrt{R_E^2 \sin^2\theta_0 + H^2 + 2R_E H} - R_E \sin\theta_0$ and $d_{\min} = H$ are the maximum and minimum distances between satellites and the user equipment, respectively.

2) Ground Stations and Communication Link

Suppose there are W GSs in the ground segments. Let $G_s = \{G_{s1}, \ldots, G_{sW}\}$ represent the set of GSs. G_{Si} signifies the ith station. Each GS serves K_M microgrids within its coverage area. Then, the total number of microgrids in the network is $K^{total} = \sum_1^W K_M$. Each GS receives operational data from microgrids, such as frequency, voltage, active power, and load status, and transmits them to satellites via the uplink. These data are then rapidly relayed across different satellites through the inter-satellite link (ISL), enabling cross-regional information forwarding. Finally, the data are delivered via the downlink to other microgrid GSs. By leveraging this end-to-end satellite-based communication architecture, geographically dispersed microgrids can achieve data sharing, state awareness, and coordinated control. This approach compensates for the lack of terrestrial network resources in certain regions, significantly enhancing the system's communication robustness and its ability to recover from disasters. All S2G links adopt multicarrier modulation with M_s subcarriers and N_s consecutive symbols. The subcarrier spacing and symbol time duration are respectively denoted as Δf and T_s, which satisfy $\Delta f = 1/T_s$.

B. Microgrid Clusters Model

In each microgrid, there exist N dispatchable inverter-based DGs, which are connected by both electrical and communication networks. In the cyber layer, a leader enables the transmission of information with other microgrid clusters via satellite internet and governs the rest of the DGs through information exchange with neighboring followers via terrestrial networks. In the physical layer, DGs are operated in a grid-forming mode to participate in voltage regulation while maintaining the power balance in the microgrid system.

The paper presents a microgrid cluster model consisting of $\mathcal{M}$ microgrids, where each microgrid can be expressed by a directed graph $\mathcal{G} = (\mathcal{V}, \mathcal{E}, \mathcal{A})$, where each DG is a node in $\mathcal{V} = \{1,2, \ldots, N\}$. A set of edges $\mathcal{E} \in \mathcal{V} \times \mathcal{V}$ defines the connections between nodes, and the weight of each node is given by the adjacency matrix $\mathcal{A} = (a_{ij})_{N\times N}$. If node i can receive information from node j, an edge $e_{ji}, \{j, i\} \in \mathcal{E}$ exists, which is indicated by $a_{ij} > 0$, while $a_{ii} = 0$ otherwise. The graph is loop-free, ensuring $a_{ii} = 0$ for all i. $N_i = \{j | a_{ij} > 0\}$ is the set of neighboring nodes i. The Laplacian matrix $\mathcal{L} = (l_{ij})$ is defined by $l_{ij} = -a_{ij}$ for $i \ne j$, and $l_{ii} = \sum_{k\ne i} a_{ik}$. Obviously, $\mathbf{1}_N^T \mathcal{L} = 0$, where $\mathbf{1}_N^T$ is a vector with dimension $N \times 1$. The edges in the form of (v_i, v_i) are called loops. $G = diag\{g_i\} \in \mathbb{R}^{N\times N}$ is denoted as a loop matrix and has at least one diagonal item as 1. A graph with loops is called a multigraph; otherwise, it is a simple graph.

The voltage droop commonly used in each DG of the DC microgrid is described as

$$V_i = V_N - R_i^v I_i, \tag{2}$$

where V_N represents the nominal voltage, and I_i is the current output of the DGi, respectively. V_i represents the output voltage of DGi. R_i^v is the virtual impedance and is usually set as $R_i^v = d_r / I_i^r$, where d_r is a design parameter and I_i^r is the rated current of the DGi. Note that $R_i^v I_i = d_r I_i / I_i^r$. Hence, achieving the proportional load sharing is equivalent to achieving the consensus in terms of $R_i^v I_i$.

However, due to its inherent characteristics, the droop control method inevitably causes voltage deviations, affecting the steady-state performance and power distribution accuracy of the system. To address this issue, secondary control is typically introduced to compensate for voltage deviations and enhance system robustness. The primary objective of secondary control is to achieve global voltage regulation while ensuring that current sharing among DGs meets the expected ratio, thereby improving the overall coordination and reliability of the system. A conventional secondary control input u_i is introduced into each DG

$$V_i = V_N - R_i^v I_i + u_i, \tag{3}$$

$$u_i = \left(k_{Pi} e_i + k_{Ii} \int e_i dt\right), \tag{4}$$

where $k_{P_i}, k_{I_i} \in \mathbb{R}^+$ are proportional and integral control coefficients. e_i are combined errors as

$$e_i = \alpha_i (V_N - \bar{V}_i) + \beta_i \sum_{j\in N_i} a_{ij}(u_j - u_i), \tag{5}$$

where $\alpha_i, \beta_i \in \mathbb{R}^+$ are error coefficients. $\bar{V}_i$ is the global average voltage value.

C. Disturbances Model of Microgrid Clusters under ISTNs

This part primarily focuses on the impact of noise and ISTN delays characteristics on system operation. For the time-domain signal $s_q(t)$ transmitted by the qth satellite, the doubly-selective faded signal received at the GS can be expressed as

$$r_q(t) = h_s s_q(t - \tau_D) + n_s(t), \tag{6}$$

where h_s is the total loss gain. $\tau_D = T_a + T_e$ is the total delay introduced by ISTNs.

Authorized licensed use limited to: HUNAN UNIVERSITY. Downloaded on September 25,2026 at 04:45:13 UTC from IEEE Xplore. Restrictions apply.
© 2026 IEEE. All rights reserved, including rights for text and data mining and training of artificial intelligence and similar technologies. Personal use is permitted, but republication/redistribution requires IEEE permission. See https://www.ieee.org/publications/rights/index.html for more information.

This article has been accepted for publication in IEEE Transactions on Smart Grid. This is the author's version which has not been fully edited and content may change prior to final publication. Citation information: DOI 10.1109/TSG.2026.3715495

1) Noise Caused by Multiple Factors

Sensors are affected by various factors, such as environmental noise, rain attenuation, electromagnetic interference, link fluctuations, and other channel uncertainties, which are often unpredictable and unavoidable. These disturbances introduce a certain degree of additive noise into the control loop [25]. Moreover, adverse weather conditions, such as rainfall, fog, and other atmospheric disturbances, can cause random perturbations to the sensors. To facilitate theoretical analysis and controller design, the overall noise considered in this paper is modeled as zero-mean additive white Gaussian noise (AWGN), i.e., $n_s(t) \sim \mathcal{N}(0, \sigma_s^2)$, where σ_s is the power spectral density of AWGN.

***Assumption 1*:** Assume that AWGN is bounded. If the noise interference becomes too large, the system will activate a protective device. Therefore, the impact of the noise signal described here can be mitigated, and stability can be restored through resilient control.

2) Loss and Interference in ISTNs

The path loss of the link between the qth satellite and the GS can be given by

$$L_q(dB) = 32.45 + 20\log_{10}(f_c) + 20\log_{10}(d) + L_{SF}, \quad (7)$$

where f_c is the carrier frequency, L_{SF} is shadowing fading loss following the normal distribution, i.e., $L_{SF} \sim N(0, \sigma_{SF}^2)$. Considering the frequency bands lower than 6 GHz, the attenuation caused by atmospheric gases, rain, and clouds can normally be neglected.

Considering that the GS is in outdoor areas, the S2G link is often accompanied by a dominant line-of-sight (LOS) path and strong Doppler shifts due to the fast movement of LEO satellites. Each S2G link comprises P propagation paths, where the Doppler tap corresponding to the pth path of the qth S2G link is denoted by $k_{p,q}$ $(p = 1, 2, \ldots, P-1)$. $k_{p,q}$ are randomly generated within the range of $[-k_{\max,q}, k_{\max,q}]$. These Doppler taps are assumed to remain constant within the duration of a single transmission frame. Specifically, the path with $p = 0$ corresponds to the LOS component. The LOS Doppler tap can be calculated by $k_{0,q} = f_D^{\max}\cos(\alpha_{0,q})N_s T_s$, where $f_D^{\max} = v_s f_c / c$ denotes the maximum Doppler shift, c is the speed of light. The angle $\alpha_{0,q}$ represents the angle between the velocity vector of the qth satellite and the line connecting the satellite to the GS. Assuming that the GS is located directly beneath the satellite orbit and the satellites move in a clockwise direction, the angle $\alpha_{0,q}$ satisfies the geometric relationship: $\cos(\alpha_{0,q}) = -\sin\psi_q / \sqrt{1 + \Upsilon^2 - 2\Upsilon\cos\psi_q}$, where $\Upsilon = (R_E + H)/R_E$. Consequently, the LOS Doppler is

$$\begin{aligned} k_{0,q} &= f_D^{\max} cos(\alpha_{0,q}) N_s T_s \\ &= -\frac{v_s f_c}{c}\left(\frac{sin\psi_q}{\sqrt{1+\Upsilon^2 - 2\Upsilon cos\psi_q}}\right) N_s T_s. \end{aligned} \quad (8)$$

Therefore, we have $h_s = \sum_0^{P-1} \sqrt{L_q} h_{p,q}\, e^{j2\pi k_{p,q} \frac{n - T_a}{M_s N_s}}$, where $h_{p,q}$ is the complex gain of the pth path of the qth S2G link, which are assumed to be time-invariant within the duration of one frame. M_s and N_s are the numbers of subcarriers and consecutive symbols, respectively.

In addition to signal attenuation, the satellite–terrestrial communication link is also affected by inter-satellite interference $I_{inter-sat}$ and ground-originated interference I_{ground}. Inter-satellite interference mainly arises from multiple satellites sharing limited spectrum resources; when different satellites operate in the same or adjacent frequency bands with overlapping coverage areas, co-channel and inter-beam interference are likely to occur. This effect becomes more significant under dense satellite constellation deployment and frequent link switching, leading to degraded received signal quality, reduced signal-to-interference-and-noise ratio, and increased decoding latency. Meanwhile, ground-originated interference is primarily caused by terrestrial wireless communication systems, fixed ground stations, or other electromagnetic emitters. Owing to spectrum coexistence and spatial coupling effects, their signals may intrude into the S2G reception process, introducing additional interference power and thereby reducing communication reliability. It should be noted that although such interference does not directly corrupt digital data, it triggers stronger channel coding, error correction, and retransmission mechanisms at the protocol layer, which in turn introduce an additional error-correction delay T_e.

3) Delays in ISTNs

The communication delay introduced by ISTNs primarily includes queueing delay T_Q, switching and processing delay T_C, transmission delay T_R, propagation delay T_P [26]. It is worth noting that this study focuses on network-layer delays introduced by the satellite segment and does not model the local access or wireless relay delays between microgrid nodes and the ground station. The end-to-end total delay for particular data can be expressed as

$$T_a = T_Q + T_C + T_R + T_P. \quad (9)$$

Queueing delay is the time data waits at communication links or switching nodes. Switching and processing delay is the time for the network device to process the packet header, determine the forwarding path, and switch the packet to the correct output channel. Transmission delay depends on link bandwidth and packet size, representing the time to enter the transmission medium. Propagation delay is determined by the electromagnetic wave speed in vacuum or atmosphere and the communication distance. In LEO networks, packet transmission delay is very small, and buffer delay within the constellation can be disregarded due to minimal inter-satellite congestion. Thus, we only consider two dominating components that contribute to end-to-end delay: switching time and signal propagation time. The former is proportional to the number of satellites traversed on the path, which depends on the satellite constellation and adopted routing method. The latter depends on orbital altitude and the number of ISL links [27].

TABLE II
MINIMUM AND MAXIMUM LEO PROPAGATION AND PROCESSING DELAY

Typical Altitude (km)	Propagation Delay (ms)	Processing Delay (ms)	Total Delay (ms)
600	4-133.8	3-42	7-175.8
1000	6.7-146.3	3-33	9.7-179.3
1400	9.3-152.8	3-27	12.3-179.8
1800	12-158.1	3-24	15-182.1
2000	13.3-150.2	3-21	16.3-171.2

Authorized licensed use limited to: HUNAN UNIVERSITY. Downloaded on September 25,2026 at 04:45:13 UTC from IEEE Xplore. Restrictions apply.
© 2026 IEEE. All rights reserved, including rights for text and data mining and training of artificial intelligence and similar technologies. Personal use is permitted, but republication/redistribution requires IEEE permission. See https://www.ieee.org/publications/rights/index.html for more information.

This article has been accepted for publication in IEEE Transactions on Smart Grid. This is the author's version which has not been fully edited and content may change prior to final publication. Citation information: DOI 10.1109/TSG.2026.3715495

***Remark 1*:** Table II presents the calculation results of the total delays for satellite networks at different altitudes [27]. Therefore, in our subsequent experiments, we will conduct experimental verification within the delay range of 10-200 ms.

III Proposed Observer-Based Distributed Resilient Control Strategy

A. Distributed Resilient Control Strategy

An observer-based distributed resilient control strategy u^W is proposed to achieve global average voltage restoration and accurate current sharing allocation for each DG. For the DGi, u_i^W is defined as

$$u_i^W(t) = k_{Wi}\int\left[k_{ei}e_i^{fd}(T_m) + u_i^F(T_m)\right]dt, \quad t \in [T_{m+1}, T_{m+2}), \tag{10}$$

where T_m denotes the sampling time at the mth instant. k_{Wi} and k_{ei} are controller gain and error gain, respectively. u_i^F is the compensator designed by the proposed distributed fault estimation observer with tunable parameters in the next section.

Considering both the noise and ISTN delays, based on (5), the dynamic error of DGi is $e_i^{fd}(t) = e_i(t)$ and the adjacent DGj $e_j^{fd}(t)$ is

$$\begin{aligned} e_j^{fd}(t) &= h_s e_j(t-\tau_D) + n_{sj}(t) \\ &= h_s\alpha_j E_j^V(t-\tau_D) \\ &\quad + h_s\beta_j\sum_{i\in\mathbf{N}_j} a_{ij}(t-\tau_D)u_{ji}^{vf}(t-\tau_D) + n_{sj}(t), \end{aligned} \tag{11}$$

where $E_i^V = V_N - \bar{V}_i$ with $\bar{V}_i(t) = V_i(t) + K_i\sum_{j\in\mathbb{N}_i} a_{ij}(t)(\bar{V}_j(t) - \bar{V}_i(t))$ and $u_{ji}^{vf} = u_j^{vf} - u_i^{vf}$. The secondary control in (4) is changed as $u_i^{vf}(t) = k_{Pi}e_i^{fd}(t-\tau_D) + k_{Ii}\int e_i^{fd}(t-\tau_D)dt$. n_{sj} is noise of DGj.

And u_i^F is designed as

$$u_i^F(t) = -\rho_i\hat{\delta}_i(t) - \hat{n}_{si}(t), \tag{12}$$

where ρ_i is the controller gain chosen by users, $\hat{\delta}_i$ and $\hat{n}_{si}$ are the estimation of δ_i and n_{si}, respectively.

As an illustrative summary, a block diagram of the designed control system is shown in Fig. 3. Here, a fault estimation observer (14) is designed for each DG, followed by calculating a distributed resilient control signal (12) to eliminate the deviation of regulation error $\hat{\delta}$. Finally, the proposed secondary control law (10) is applied to each DG against noise and ISTN delays simultaneously. In the next subsection, a design method of a distributed fault estimation observer with tunable parameters is introduced.

B. Distributed Fault Estimation Observer with Tunable Parameters

The real regulation error δ_i of the DGi is defined as

$$\delta_i = \bar{V}_i - V_N + R_i^v I_i - \lambda_N, \tag{13}$$

where λ_N is the optimal value of $R_i^v I_i$ at the steady state.

To address the effect of noise and inspired by [28], a distributed fault estimation observer is proposed in each DG, and the observer model with N DGs is designed as

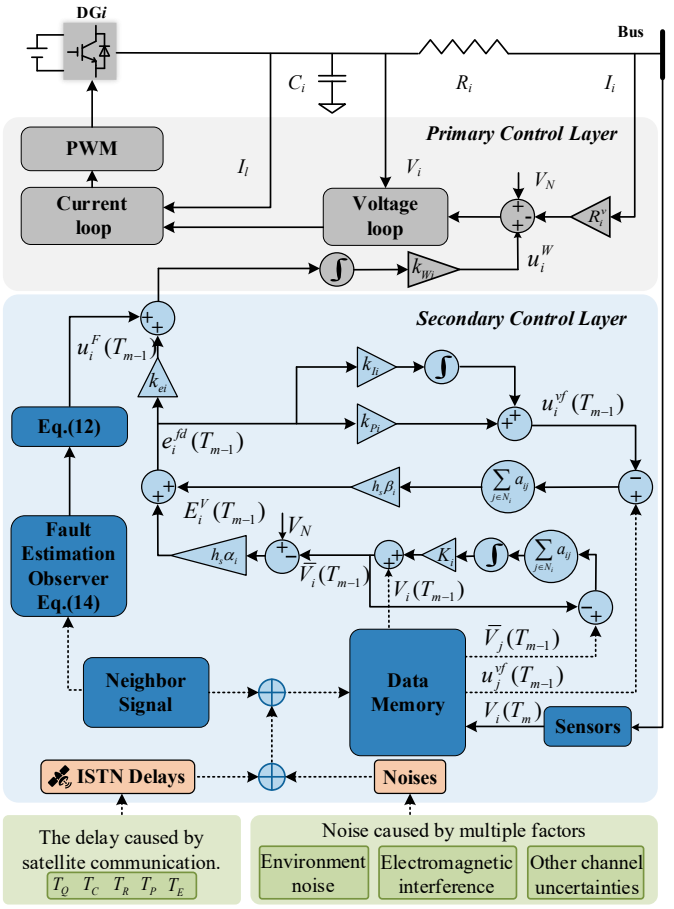


Fig. 3. The diagram of the proposed distributed resilient control strategy.

$$\begin{cases} \dot{\hat{\delta}}(t) = -K(\mathcal{L}+G)\hat{\delta}(t) + u^F(t) + \hat{n}_s(t) - H_1\varepsilon(t) \\ \hat{n}_s(t) = -H_2\int_{t_f}^{t}\varepsilon(\tau)d\tau - \mu F\varepsilon(t) \end{cases}, \tag{14}$$

where $\hat{\delta} = [\hat{\delta}_1, \dots, \hat{\delta}_N]^T$, $u^F = [u_1^F, \dots, u_N^F]^T$, $\hat{n}_s = [\hat{n}_{s1}, \dots, \hat{n}_{sN}]^T$, $\varepsilon = [\varepsilon_1, \dots, \varepsilon_N]^T$, $K = diag(k_i)$ and $G = diag(g_i)$. t_f represents the moment when the noise estimation module is activated, u^F is an additional distributed resilient control input signal for compensating the effects of noise. H_1 and H_2 are the observer gain matrices, which need to be designed. $\mu F\dot{\varepsilon}(t)$ represents an adjustable parameter to improve robustness, where μ is a constant and F is a tunable parameter matrix. The relative output estimation error for the ith node is defined as

$$\begin{aligned} \varepsilon_i(t) = &\sum_{j\in N_i} a_{ij}((\hat{\delta}_i(t) - \delta_i(t)) - (\hat{\delta}_j(t) - \delta_j(t))) \\ &+ g_i(\hat{\delta}_i(t) - \delta_i(t)), \end{aligned} \tag{15}$$

where a_{ij} and g_i represent the element values of the matrix $\mathcal{A}$ and the loop-graph matrix G, respectively.

***Assumption 2*:** For δ_i and e_n with $\delta_i = 0$ and $e_n = 0$, there exist nonnegative constants q_{V1i} and q_{V2i} such that for $\forall t > 0$, $\|\delta_i\| < q_{V1i}$ and $\|e_n\| < q_{V2i}$.

C. Observer Gain Calculation Based on H_∞ Performance

For the DGi, the fault estimation observer (14) can be rewritten in the following form

Authorized licensed use limited to: HUNAN UNIVERSITY. Downloaded on September 25,2026 at 04:45:13 UTC from IEEE Xplore. Restrictions apply.
© 2026 IEEE. All rights reserved, including rights for text and data mining and training of artificial intelligence and similar technologies. Personal use is permitted, but republication/redistribution requires IEEE permission. See https://www.ieee.org/publications/rights/index.html for more information.

This article has been accepted for publication in IEEE Transactions on Smart Grid. This is the author's version which has not been fully edited and content may change prior to final publication. Citation information: DOI 10.1109/TSG.2026.3715495

$$\dot{\hat{\mathrm{X}}}(t)=A\hat{\mathrm{X}}(t)+Bu^{F}(t)-\bar{H}\varepsilon(t)-\mu\bar{F}\dot{\varepsilon}(t), \tag{16}$$

where

$$\hat{\mathrm{X}}(t)=\begin{bmatrix}\hat{\delta}(t)\\ \hat{n}_s(t)\end{bmatrix},$$

$$A=\begin{bmatrix}-K(\mathcal{L}+G) & I_N\\ 0_{N\times N} & 0_{N\times N}\end{bmatrix}, B=\begin{bmatrix}I_N\\ 0_{N\times N}\end{bmatrix}, \bar{H}=\begin{bmatrix}H_1\\ H_2\end{bmatrix}, \bar{F}=\begin{bmatrix}0_{N\times N}\\ F\end{bmatrix},$$

where $I_N = diag(N)$, $H_1 = I_N \otimes h_1$, $H_2 = I_N \otimes h_2$, $F = I_N \otimes f$, and $\otimes$ represents the Kronecker product.

Then, the error matrix of the DGi is defined as follows:

$$e_{\mathrm{X}}(t)=\hat{\mathrm{X}}(t)-\mathrm{X}(t), \tag{17}$$

$$e_{\delta}(t)=\hat{\delta}(t)-\delta(t), \tag{18}$$

$$e_{n}(t)=\hat{n}(t)-n(t). \tag{19}$$

Based on (13), the derivative of δ_i is obtained as:

$$\dot{\delta}_i=K_i\Big[\sum_{j\in\mathbf{N}_i}(\delta_j-\delta_i)-g_i\delta_i\Big]+\dot{n}_{si}(t)+u_i^{F}(t). \tag{20}$$

Also, rewriting (20), we can obtain

$$\dot{\mathrm{X}}(t)=A\mathrm{X}(t)+Bu^{F}(t)+D\dot{n}_s(t), \tag{21}$$

where $\mathrm{X}=[\delta(t)\quad n_s(t)]^T$. $D=[0_{N\times N}\quad I_N]^T$.

From (15), we obtain

$$\varepsilon(t)=(\mathcal{L}+G)e_{\delta}(t)=(\mathcal{L}+G)Je_{\mathrm{X}}(t), \tag{22}$$

where $J=[I_N\quad 0_{N\times N}]$.

Then we can obtain the derivative of global state error $e_{\mathrm{X}}(t)$,

$$\begin{aligned}\dot{e}_{\mathrm{X}}(t)&=\dot{\hat{\mathrm{X}}}(t)-\dot{\mathrm{X}}(t)\\ &=Ae_{\mathrm{X}}(t)-D\dot{n}_S(t)-\Big((\mathcal{L}+G)\Big(\bar{H}J\Big)\Big)e_{\mathrm{X}}(t)\\ &\quad-\Big((\mathcal{L}+G)\Big(\mu\bar{F}J\Big)\Big)\dot{e}_{\mathrm{X}}(t).\end{aligned} \tag{23}$$

Furthermore, we obtain

$$Q\dot{e}_{\mathrm{X}}(t)=\Big(A-(\mathcal{L}+G)\Big(\bar{H}J\Big)\Big)e_{\mathrm{X}}(t)-D\dot{n}_s(t), \tag{24}$$

where $Q=[I+(\mathcal{L}+G)(\mu\bar{F}J)]$ and it is nonsingular since $\bar{F}J=\begin{bmatrix}0\\ F\end{bmatrix}[I_N\quad 0]=\begin{bmatrix}0 & 0\\ F & 0\end{bmatrix}$.

Obviously, we obtain

$$\dot{e}_{\mathrm{X}}(t)=Q^{-1}\Big(A-(\mathcal{L}+G)\Big(\bar{H}J\Big)\Big)e_{\mathrm{X}}(t)-Q^{-1}D\dot{n}_s(t), \tag{25}$$

and the noise estimation error is

$$e_n(t)=\begin{bmatrix}0 & I_N\end{bmatrix}e_{\mathrm{X}}(t). \tag{26}$$

To enhance the accuracy of the fault estimation observer under noise and ensure the transient performance of the system, we calculate the H_∞ performance of the observer gain $\bar{H}$. Additionally, H_∞ constraints are introduced to mitigate the impact of $\dot{n}_s(t)$ on noise estimation errors.

Lemma 1: The eigenvalues of a given matrix $\mathcal{B}\in\mathbb{R}^{n\times n}$ belong to the circular region $\mathcal{D}(\sigma,\tau)$ with center $\sigma+j0$ and radius τ if and only if there exists a symmetric positive definite matrix $\mathcal{P}\in\mathbb{R}^{n\times n}$ satisfying $\begin{bmatrix}-\mathcal{P} & \mathcal{P}(\mathcal{B}-\sigma I_n)\\ * & -\tau^2\mathcal{P}\end{bmatrix}<0$.

***Theorem 1*:** Given a performance level γ_p and a circular region $\mathcal{D}(\sigma,\tau)$, for a given matrix Q, if there exist a symmetric positive definite matrix $\bar{P}\in\mathbb{R}^{2N\times 2N}$ and a matrix $\bar{Y}\in\mathbb{R}^{2N\times N}$ such that

$$\begin{bmatrix}\phi & -Q^{\mathrm{T}}\bar{P}D & I_N\otimes\bar{I}_r^{\mathrm{T}}\\ * & -\gamma & 0\\ * & * & -\gamma\end{bmatrix}<0, \tag{27}$$

$$\begin{bmatrix}-\bar{P} & \Theta\\ * & -\tau^2Q^{\mathrm{T}}\bar{P}Q\end{bmatrix}<0, \tag{28}$$

where $\phi=Q^{\mathrm{T}}(\bar{P}A-(\mathcal{L}+G)(\bar{Y}J))+(A^{\mathrm{T}}\bar{P}(\mathcal{L}+G)^{\mathrm{T}}(J^{\mathrm{T}}\bar{Y}^{\mathrm{T}}))Q$, $\Theta=\bar{P}A-(\mathcal{L}+G)(\bar{Y}J)-\sigma\bar{P}Q$ and $\bar{I}_r=[0\quad 1]$. Then (25) and (26) satisfy the H_∞ performance $\|T_{\dot{n}_s(t)e_n(t)}\|_\infty<\gamma$ and the eigenvalues of $Q^{-1}(A-(\mathcal{L}+G)(\bar{H}J))$ belong to $\mathcal{D}(\sigma,\tau)$. The observer gain $\bar{H}$ is given by $\bar{H}=\bar{P}^{-1}\bar{Y}$.

Proof. We first prove (27). Since Q is nonsingular, for a symmetric positive definite $\bar{P}$, it concludes that $Q^T\bar{P}Q$ is also a symmetric positive definite. By choosing the Lyapunov function

$$V_1(t)=e_{\mathrm{X}}^{\mathrm{T}}(t)\Big(Q^{\mathrm{T}}\bar{P}Q\Big)e_{\mathrm{X}}(t), \tag{29}$$

and using the bounded real lemmas for continuous-time systems, one directly obtains that if condition (27) holds, the (25) and (26) satisfy the H_∞ performance $\|T_{\dot{n}_s(t)e_n(t)}\|_\infty<\gamma$.

Then, for a symmetric positive definite $Q^T\bar{P}Q$ and a circular region $\mathcal{D}(\sigma,\tau)$, if condition

$$\begin{bmatrix}Q^{\mathrm{T}}\big(-\bar{P}\big)Q & Q^{\mathrm{T}}\Theta\\ * & -\tau^2Q^{\mathrm{T}}\bar{P}Q\end{bmatrix}<0 \tag{30}$$

holds based on Lemma 1, then the eigenvalues of $Q^{-1}(A-(\mathcal{L}+G)(\bar{H}J))$ belong to $\mathcal{D}(\sigma,\tau)$. Furthermore, if (30) is feasible, then pre-multiplying and post-multiplying by $\begin{bmatrix}Q^{-T} & 0\\ 0 & I\end{bmatrix}$ and its transpose, we get (28) directly.

***Remark 2*:** For (25), the first step is to determine matrix $[I+(\mathcal{L}+G)(\mu\bar{F}J)]$. Generally, the selection of adjustable parameters is that F initially is chosen as a row full-rank matrix, which may lead to a lower H_∞ performance level γ. Then we can try different parameter μ to get the H_∞ performance level γ as small as possible. Therefore, the matrix Q is known before calculating observer gain $\bar{H}$.

Once the matrix is established, the conditions in Theorem 1 are expressed in terms of LMIs. A common Lyapunov matrix is employed for both conditions (27) and (28), introducing some design conservatism. To mitigate this conservatism, a modified approach is proposed, suggesting the use of distinct Lyapunov matrices for the two conditions.

***Theorem 2*:** Given a H_∞ performance level γ and a circular region $\mathcal{D}(\sigma,\tau)$. For a prescribed matrix Q and a scalar ζ, if there exist symmetric positive definite matrices $\bar{P}_1,\bar{P}_2\in\mathbb{R}^{2N\times 2N}$ and matrices $\bar{S}\in\mathbb{R}^{2N\times 2N}$, $\bar{Y}\in\mathbb{R}^{2N\times N}$ satisfying

$$\begin{bmatrix}\phi_{11} & \phi_{12} & -Q^{\mathrm{T}}\big(\bar{S}D\big) & I_N\otimes\bar{I}_r^{\mathrm{T}}\\ * & \phi_{22} & -\zeta Q^{\mathrm{T}}\big(\bar{S}D\big) & 0\\ * & * & -\gamma & 0\\ * & * & * & -\gamma\end{bmatrix}<0, \tag{31}$$

Authorized licensed use limited to: HUNAN UNIVERSITY. Downloaded on September 25,2026 at 04:45:13 UTC from IEEE Xplore. Restrictions apply.
© 2026 IEEE. All rights reserved, including rights for text and data mining and training of artificial intelligence and similar technologies. Personal use is permitted, but republication/redistribution requires IEEE permission. See https://www.ieee.org/publications/rights/index.html for more information.

This article has been accepted for publication in IEEE Transactions on Smart Grid. This is the author's version which has not been fully edited and content may change prior to final publication. Citation information: DOI 10.1109/TSG.2026.3715495

$$\begin{bmatrix} \bar{P}_2 - \bar{S} - \bar{S}^{\mathrm{T}} & \Theta \\ * & -\tau^2 Q^{\mathrm{T}} \bar{P}_2 Q \end{bmatrix} < 0, \tag{32}$$

where $\phi_{11} = Q^{\mathrm{T}}(\bar{S}A - (\mathcal{L}+G)(\bar{Y}J)) + (A^{\mathrm{T}}\bar{S}^{\mathrm{T}} - (\mathcal{L}+G)^{\mathrm{T}}(J^{\mathrm{T}}\bar{Y}^{\mathrm{T}}))Q$, $\phi_{12} = Q^{\mathrm{T}}(\bar{P}_1 - \bar{S})M + \zeta(A^{\mathrm{T}}\bar{S}^{\mathrm{T}} - (\mathcal{L}+G)^{\mathrm{T}}J^{\mathrm{T}}\bar{Y}^{\mathrm{T}})Q$, $\phi_{22} = -\zeta Q^{\mathrm{T}}(\bar{S}+\bar{S}^{\mathrm{T}})Q$ and $\Theta = \bar{S}A - (\mathcal{L}+G)(\bar{Y}J) - \sigma\bar{S}Q$. Then (25) and (26) satisfy the H_∞ performance $\left\|T_{\dot{n}_s(t)e_n(t)}\right\|_\infty < \gamma$ and the eigenvalues of $Q^{-1}(A-(\mathcal{L}+G)(\bar{H}J))$ belong to $\mathcal{D}(\sigma,\tau)$. The observer gain $\bar{H}$ is given by $\bar{H} = \bar{S}^{-1}\bar{Y}$.

Proof. For conditions of Theorem 2, different Lyapunov matrices $Q^T\bar{P}_1Q$ and $Q^T\bar{P}_2Q$ are introduced. Based on the proof of Theorem 1, here we only need to prove that (31) is equivalent to (27) when setting $\bar{P}_1 = \bar{P}$, and (32) is equivalent to (28) when setting $\bar{P}_2 = \bar{P}$.

If (31) is feasible, then pre- and post-multiplying by

$$\begin{bmatrix} I & \left(A-(\mathcal{L}+G)(\bar{H}J)\right)^{\mathrm{T}} Q^{-\mathrm{T}} & 0 & 0 \\ 0 & -D^{\mathrm{T}}Q^{-\mathrm{T}} & I & 0 \\ 0 & 0 & 0 & I \end{bmatrix}, \tag{33}$$

and its transpose, we can get (32) directly.

From $\bar{S}+\bar{S}^T \geq \bar{P} > 0$, $\bar{S}$ is nonsingular. Since $\bar{P}$ is symmetric positive definite, the inequality $(\bar{P}-\bar{S})\bar{P}^{-1}(\bar{P}-\bar{S})^T$ holds and it can also be expressed as $-\bar{S}-\bar{S}^T+\bar{P} \geq -\bar{S}\bar{P}^{-1}\bar{S}^T$. Therefore, it follows from (31) that

$$\begin{bmatrix} -\bar{S}\bar{P}^{-1}\bar{S}^{\mathrm{T}} & \Theta \\ * & -\tau^2 Q^{\mathrm{T}}\bar{P}Q \end{bmatrix} < 0. \tag{34}$$

Then pre- and post-multiplying by

$$\begin{bmatrix} \bar{P}\bar{S}^{-1} & 0 \\ * & I \end{bmatrix} \tag{35}$$

and its transpose, we can get (28), proving that (32) is equivalent to (28).

D. System Stability Analysis

A global tracking error model is established, and its stability is derived through theoretical analysis. It is proven that the proposed method can realize global voltage regulation and ensure that the current sharing among DGs conforms to the expected ratio.

***Theorem 3*:** Based on Assumption 1 and Theorems 1-2, for given positive definite matrices J_1, J_2 and $\eta > 0$ with the proposed control strategy (10), the average voltage restoration and accurate current sharing of remote microgrid clusters can be achieved simultaneously under noise and delays.

Proof. By choosing the Lyapunov function

$$V_2(t) = \delta^T(t)J_1\delta(t) + e_\delta^{\mathrm{T}}(t)J_2e_\delta(t), \tag{36}$$

where J_1, J_2 are positive definite matrices.

$$\dot{\delta} = \left(\mathrm{T}-\rho\right)\delta - \rho e_\delta - e_n, \tag{37}$$

$$\dot{e}_\delta = \left(\mathrm{T}-H_1(\mathcal{L}+G)\right)e_\delta + e_n, \tag{38}$$

where $\mathrm{T} = -K(\mathcal{L}+G)$.

Accordingly, we can obtain

$$\begin{aligned} \dot{V}_2(t) = {} & \delta^T\left(J_1\left(\mathrm{T}-\rho\right)+\left(\mathrm{T}-\rho\right)^T J_1\right)\delta - 2\delta^T J_1\rho e_\delta \\ & -2\delta^T J_1 e_n + e_\delta{}^T\left(J_2\overline{\mathrm{T}}+\overline{\mathrm{T}}^T J_2\right)e_\delta + 2e_\delta{}^T J_2 e_n, \end{aligned} \tag{39}$$

where $\overline{\mathrm{T}} = \mathrm{T} - H_1(\mathcal{L}+G)$.

According to Assumption 2, we have

$$-2\delta^T J_1 e_n \leq \frac{1}{\eta}\delta^T J_1 J_1^T \delta + \eta q_{V1}^2, \tag{40}$$

$$2e_\delta{}^T J_2 e_n \leq \frac{1}{\eta} e_\delta{}^T J_2 J_2^T e_\delta + \eta q_{V2}^2, \tag{41}$$

where η is constant. $q_{V1} = diag(q_{V1i})$ and $q_{V2} = diag(q_{V2i})$.

Combining (39)- (41) yields

$$\begin{aligned} \dot{V}_2(t) \leq {} & \delta^T\left(J_1\left(\mathrm{T}-\rho\right)+\left(\mathrm{T}-\rho\right)^T J_1\right)\delta - 2\delta^T J_1\rho e_\delta \\ & + \frac{1}{\eta}\delta^T J_1 J_1^T\delta + \eta q_{V1}^2 + e_\delta{}^T\left(J_2\overline{\mathrm{T}}+\overline{\mathrm{T}}^T J_2\right)e_\delta \\ & + \frac{1}{\eta} e_\delta{}^T J_2 J_2^T e_\delta + \eta q_{V2}^2. \end{aligned} \tag{42}$$

Define $\Xi(t) = [\delta^T(t), e_\delta^T(t)]^T$. Then, (42) can be rewritten as

$$\dot{V}_2(t) \leq \Xi^T\Gamma\Xi + \eta q_{V1}^2 + \eta q_{V2}^2, \tag{43}$$

where $\Gamma = \left[\Gamma_{ij}\right] \in \mathbb{R}^{2N\times 2N}$ is given as $\Gamma_{11} = J_1(T-\rho) + (T-\rho)^T J_1 + \frac{1}{\eta}J_1J_1^T$, $\Gamma_{12} = \Gamma_{21}^T = -J_1\rho$, $\Gamma_{22} \equiv J_2\overline{T} + \overline{T}^T J_2 + \frac{1}{\eta}J_2J_2^T$.

From (36), it can be found that

$$V_2(t) \leq \max(\lambda_{\max}(J_1), \lambda_{\max}(J_2))\Xi^T\Xi, \tag{44}$$

where $\lambda_{\max}(\cdot)$ represents the maximum eigenvalue of the matrix. Thus, by applying the Schur complement lemma and substituting (44) into (43), we have

$$\dot{V}_2(t) \leq -\kappa V_2(t) + \xi, \tag{45}$$

where $\kappa = \frac{\min(-\Gamma)}{\max(\lambda_{\max}(J_1),\lambda_{\max}(J_2))}$, $\min(-\Gamma)$ is the minimum component in the matrix $-\Gamma$ and $\xi = \eta q_{V1}^2 + \eta q_{V2}^2$.

Define a set $E = \left\{\Xi(t)\left|\lambda_{\max}(J_1)\parallel\delta\parallel + \lambda_{max}(J_2)\|e_\delta\| \geq \frac{\xi}{\kappa}\right.\right\}$ and E^S is the complementary set of E, then we obtain

$$V_2(t) \geq \lambda_{max}(J_1)\left\|\delta(t)\right\|^2 + \lambda_{max}(J_2)\left\|e_\delta(t)\right\|^2 \geq \frac{\xi}{\kappa}. \tag{46}$$

If $\Xi \in E^S$, according to the Lyapunov theory, Ξconverges exponentially to E.

According to the above analysis, we obtain

$$\lim_{t\to\infty} e_\delta(t) = 0, \tag{47}$$

$$\lim_{t\to\infty} \delta(t) = 0. \tag{48}$$

Under Theorems 1-2, we obtain

$$\lim_{t\to\infty} e_n = 0, \tag{49}$$

which indicates the proposed observer can estimate the fault signals successfully.

Additionally, according to (48), we have

$$\lim_{t\to\infty} -GE^V(t) = \lim_{t\to\infty}\mathcal{L}\left(\bar{V}(t) + Z(\lambda(t)-\lambda_N)\right), \tag{50}$$

where $E^V(t) = [E_1^V(t),\ldots,E_N^V(t)]^T$, $\bar{V} = [\bar{V}_1(t),\ldots,\bar{V}_N(t)]^T$,

Authorized licensed use limited to: HUNAN UNIVERSITY. Downloaded on September 25,2026 at 04:45:13 UTC from IEEE Xplore. Restrictions apply.
© 2026 IEEE. All rights reserved, including rights for text and data mining and training of artificial intelligence and similar technologies. Personal use is permitted, but republication/redistribution requires IEEE permission. See https://www.ieee.org/publications/rights/index.html for more information.

This article has been accepted for publication in IEEE Transactions on Smart Grid. This is the author's version which has not been fully edited and content may change prior to final publication. Citation information: DOI 10.1109/TSG.2026.3715495

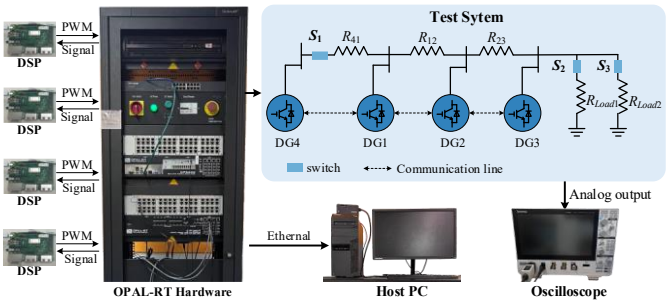


Fig. 4. The schematic diagram of the test microgrid system.

TABLE III
PARAMETERS OF THE MICROGRID AND THE CONTROLLERS

DG1/DG2/DG3/DG4	
DC Side Voltage	V_{dc}=100V
Pulse Frequency	f_S=20kHz
Nominal Voltage	$V_N = 48V$
Virtual Impedance	$R_1^v = 8, R_2^v = 4, R_3^v = 2, R_4^v = 2$
Line Resistance	$R_{12} = 0.1\Omega, R_{23} = 0.1\Omega, R_{41} = 0.1\Omega$
Proposed Controller	
Error Coefficients	$\alpha_1 = 10, \alpha_2 = 10, \alpha_3 = 10, \alpha_4 = 10$ $\beta_1 = 1, \beta_2 = 1, \beta_3 = 1, \beta_4 = 1$ $g_1 = 1, g_2 = 1, g_3 = 1, g_4 = 1$
Controller Gain	$\rho_1 = 3, \rho_2 = 2, \rho_3 = 1, \rho_4 = 1$

$\lambda(t) = R_i^v I_i - \lambda_N$ and $Z = [Z_{ij}]$. For $i = j$, we have $Z_{ij} = 1 - g_i/|N_i|$; for $\forall i, j = 1, \ldots, N$ and $i \neq j$, $Z_{ij} = 1$.

Multiplying $\mathbf{1}_N^T$ on both sides of (50), we have

$$\lim_{t\to\infty} -\mathbf{1}_N^T G E^V(t) = \lim_{t\to\infty} \mathbf{1}_N^T \mathcal{L}\left(\bar{V}(t) + Z(\lambda(t) - \lambda_N)\right). \quad (51)$$

As $\mathbf{1}_N^T \mathcal{L} = 0$ and $\mathbf{1}_N^T G \neq 0$, by choosing proper G, we obtain

$$\lim_{t\to\infty} E^V(t) = 0. \quad (52)$$

Based on (48) and (52), we have

$$\lim_{t\to\infty} \lambda(t) = \lambda_N. \quad (53)$$

Eq. (52) indicates that the proposed resilient controller can ultimately restore the DC bus voltage to its reference value. In conjunction with (53), this implies that the system can also achieve the control objective of accurate current distribution.

IV CASE STUDIES

To evaluate the effectiveness and resilience of the proposed observer-based distributed resilient control strategy, this paper selects a DC microgrid containing 4 DGs as an example and conducts experiments using the real-time simulator OPAL-RT, as shown in Fig. 4. Each DG unit comprises a DC power source, a boost DC/DC converter, and an LC filter. Additionally, the system configuration can be flexibly adjusted by controlling three circuit breakers ($S1$–$S3$), allowing various operational scenarios to be tested. The microgrid's communication network topology, depicted in Fig. 4, follows a fully connected graph structure, ensuring robust information exchange among DGs. The key system parameters and controller settings are detailed in Table III, providing a comprehensive overview of the experimental setup. The noise intensity does not replicate specific modulation noise power but represents moderate-to-severe disturbances like noise, fading, and interference in satellite-aided remote microgrids in order to evaluate the controller's robustness and stability.

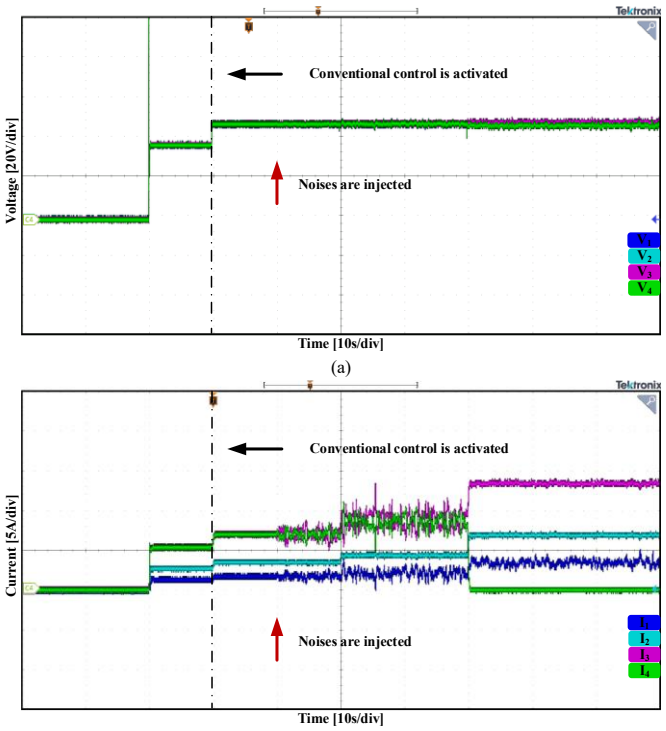


Fig. 5. System outputs performance of the conventional control strategy under noise. (a) Voltage. (b) Current.

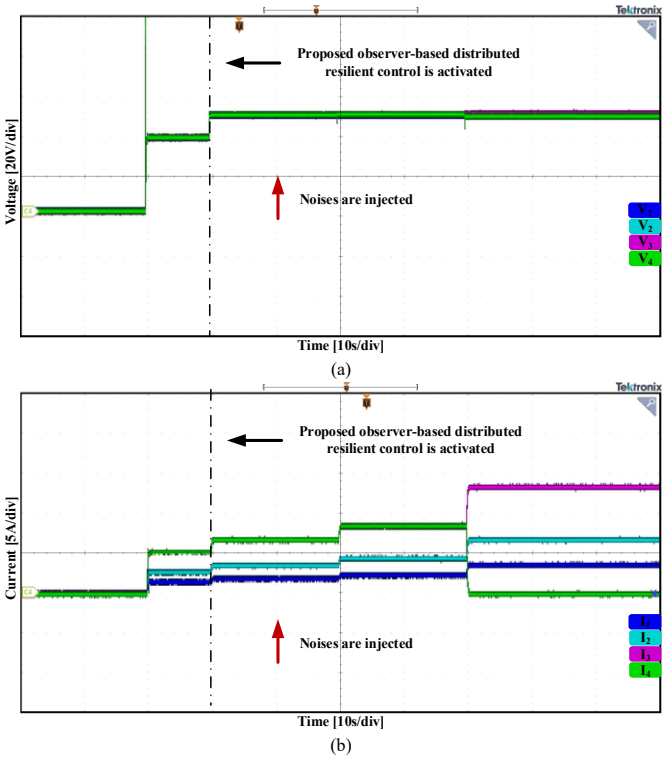


Fig. 6. System outputs performance of the proposed control strategy under noise. (a) Voltage. (b) Current.

The initial rated voltage is set to 48 V, with the current distribution among the four units as follows: $I_1 : I_2 : I_3 : I_4 = 1 : 2 : 4 : 4$. To assess the performance of the controller under

Authorized licensed use limited to: HUNAN UNIVERSITY. Downloaded on September 25,2026 at 04:45:13 UTC from IEEE Xplore. Restrictions apply.
© 2026 IEEE. All rights reserved, including rights for text and data mining and training of artificial intelligence and similar technologies. Personal use is permitted, but republication/redistribution requires IEEE permission. See https://www.ieee.org/publications/rights/index.html for more information.

This article has been accepted for publication in IEEE Transactions on Smart Grid. This is the author's version which has not been fully edited and content may change prior to final publication. Citation information: DOI 10.1109/TSG.2026.3715495

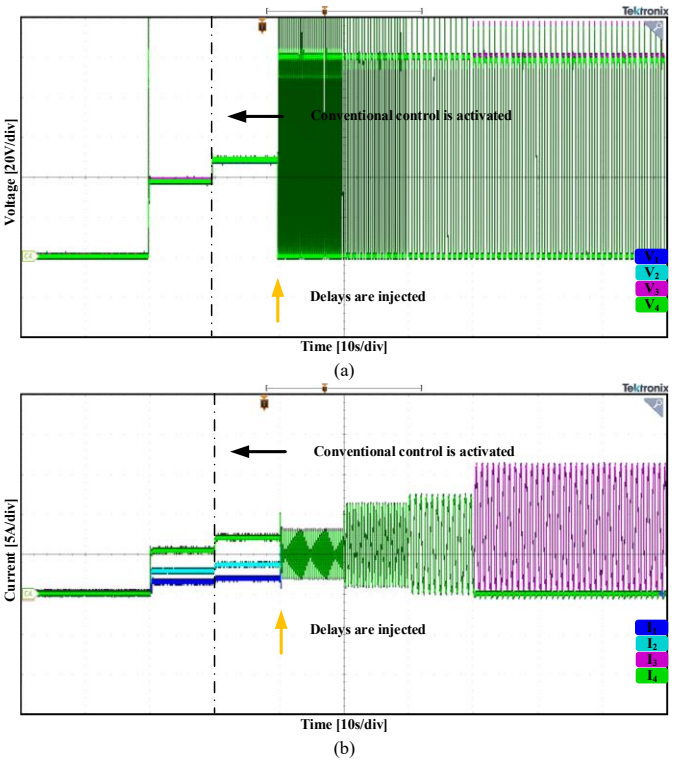


Fig. 7. System outputs performance of the conventional control strategy under ISTNs delays. (a) Voltage. (b) Current.

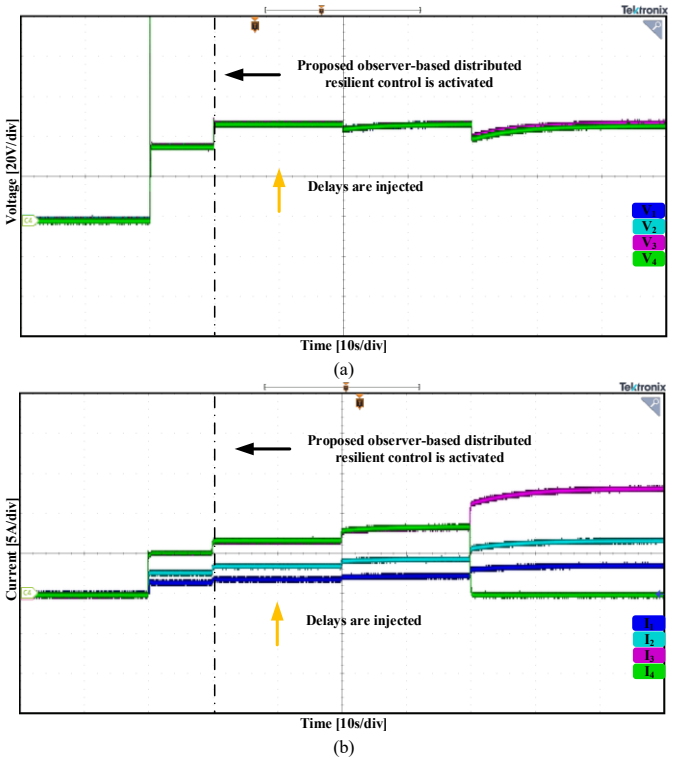


Fig. 8. System outputs performance of the proposed control strategy under ISTN delays. (a) Voltage. (b) Current.

different operating conditions, the following events are introduced in succession:

(1) At t = 10 s, the secondary control is activated.
(2) At t = 30 s, an extra R_{load1} (10 Ω) is added.
(3) At t = 50 s, DG4 is removed from the microgrid.

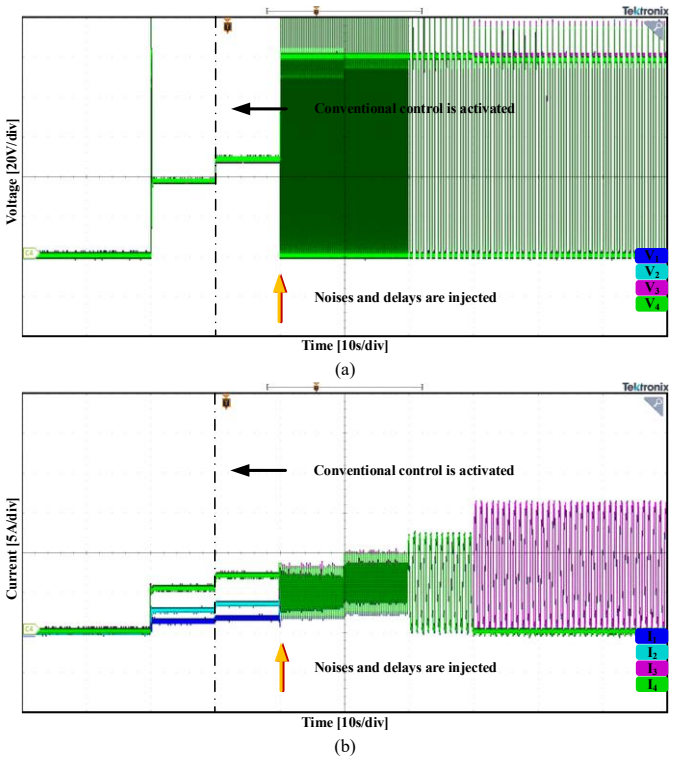


Fig. 9. System outputs performance of the conventional control strategy under noise and ISTN delays. (a) Voltage. (b) Current.

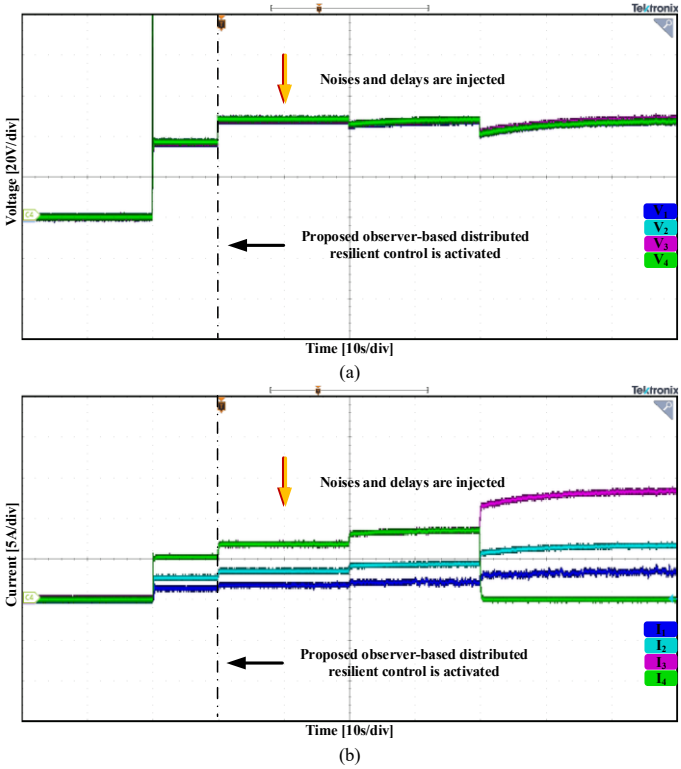


Fig. 10. System outputs performance of the proposed control strategy under noise and ISTN delays. (a) Voltage. (b) Current.

These sequential disturbances are designed to thoroughly test the resilience of the proposed control strategy, ensuring that the system can maintain stable voltage levels and proper current-sharing ratios under varying conditions.

Authorized licensed use limited to: HUNAN UNIVERSITY. Downloaded on September 25,2026 at 04:45:13 UTC from IEEE Xplore. Restrictions apply.
© 2026 IEEE. All rights reserved, including rights for text and data mining and training of artificial intelligence and similar technologies. Personal use is permitted, but republication/redistribution requires IEEE permission. See https://www.ieee.org/publications/rights/index.html for more information.

This article has been accepted for publication in IEEE Transactions on Smart Grid. This is the author's version which has not been fully edited and content may change prior to final publication. Citation information: DOI 10.1109/TSG.2026.3715495

A. Distributed Resilient Control Strategy under Noise

In this case, the noise is set as: (1) At t = 20s, σ_s= 2. (2) At t = 30s, σ_s= 3. (3) At t = 40s, σ_s= 6. Fig. 5 shows the variations in the DG bus voltage and output current under the conventional secondary control strategy when noise is injected. When the secondary control is activated at t = 10s, the average bus voltage stabilizes at 48V, and the output currents follow the inverse proportion of droop coefficients: $I_1 : I_2 : I_3 : I_4 = 1 : 2 : 4 : 4$. At t = 20s, noise is injected into the model, resulting in voltage and current fluctuations across DGs in the microgrid. Without the proposed control strategy, the system exhibits increasingly severe voltage and current disturbances as the noise intensity grows, indicating pronounced instability. In contrast, Fig. 6 illustrates the system response under the proposed control strategy. Compared to Fig. 5, the voltage profiles of all DGs are more stable and become more controllable, with smoother waveforms that return to steady state more rapidly and are nearly unaffected by the intensified noise. The regulation of voltage and current rapidly follows the initial disturbance, demonstrating enhanced operational robustness. From a system-level perspective, the proposed control strategy effectively mitigates the impact of noise interference, resulting in reduced degradation of dynamic performance. This confirms the effectiveness of the proposed method in suppressing noise-induced disturbances and improving the overall stability of the microgrid system.

B. Distributed Resilient Control Strategy under Delays

In this case, the communication link 1-2 is injected with delays. To simulate the variation and magnitude of the delays under ISTN, the delay is gradually increased and set as: (1) At t = 20s, τ_D=50ms. (2) At t = 30s, τ_D=100ms. (3) At t = 40s, τ_D=200ms.

Fig. 7 depicts the impact of ISTN delays on the voltage and current of DGs, where the gradually increasing delay affects the reception of signals from adjacent units by each DG. The voltage and current of each DG become unstable with visible oscillations. These disruptions suggest that the delays in communication between these DGs are influencing their operational stability. In addition, Fig. 8 shows the performance of the proposed control strategy against such delays. The output of each DG is no longer oscillating, with a relatively stable voltage and a smoother current curve. Moreover, with the increase of signal delay, the controller can still ensure the stable operation of the microgrid, proving that the proposed control method can effectively suppress the negative impact of time-varying communication delay on the microgrid.

C. Distributed Resilient Control Strategy under Both Noise and ISTN Delays

In this case, the effectiveness of the designed control strategy in mitigating the impact of both noise and ISTN delays is thoroughly evaluated. The experimental setup is: (1) At t = 20s, σ_s= 1, τ_D=50ms. (2) At t = 40s, σ_s= 2, τ_D=200ms. Fig. 9 shows that when the system is subjected to time delay and noise injection, the voltage and current are not only disturbed but also exhibit oscillations. In Fig. 10, after adopting the proposed control strategy and activating the secondary control, despite the impact of noise and ISTN delays, the voltage and current of the four DGs recover at a slower rate. Nevertheless, the global average voltage ultimately stabilizes at 48 V, and satisfactory current sharing among the DGs is achieved.

Furthermore, we conducted additional tests to evaluate the robustness limits of the proposed controller, showing that it can tolerate a maximum noise level of σ_s =6 and a maximum delay of τ_D =400 ms. These results verify the effectiveness of the proposed control strategy in maintaining system stability in the presence of noise and ISTN delays.

V Conclusion

In this paper, an observer-based distributed resilient control strategy is proposed to address the challenges posed by noise and ISTN delays in remote microgrid clusters. The proposed method introduces an observer based on tunable parameters that effectively estimates microgrid cluster states under varying noise. By integrating the designed observer with a distributed resilient control strategy, the system ensures global voltage restoration and accurate current sharing, even when noise and ISTN delays are considered simultaneously. Theoretical analysis and experimental verification validate that the proposed strategy maintains stability and enhances system robustness under various operational scenarios.

With the growing reliance on remote microgrids under ISTNs, future research will focus on enhancing the adaptability of microgrid clusters under highly dynamic ISTN conditions. This includes refining observer models to accommodate more complex stochastic noise patterns and developing an advanced cybersecurity framework to address potential cyber threats in satellite-terrestrial communications and further support the integration of distributed renewable energy resources in challenging environments.

References

[1] S. Tan et al., "Lyapunov-based resilient cooperative control for DC microgrid clusters against false data injection cyber-attacks," *IEEE Trans. Smart Grid*, vol. 15, no. 3, pp. 3208–3222, May 2024.

[2] C. Zhang, X. Dou, L. Wang, Y. Dong, and Y. Ji, "Distributed cooperative voltage control for grid-following and grid-forming distributed generators in islanded microgrids," *IEEE Trans. Power Syst*., vol. 38, no. 1, pp. 589–602, Jan. 2023.

[3] X. Zhu and C. Jiang, "Integrated satellite-terrestrial networks toward 6G: Architectures, applications, and challenges," *IEEE Internet Things J*., vol. 9, no. 1, pp. 437–461, Jan. 2022.

[4] Y. Shen et al., "LEO Satellite Internet Assisted Data-Driven Predictive Control for Remote Islanded Microgrid Stability Enhancement," *IEEE Trans. Ind. Appl.*, vol. 60, no. 3, pp. 4557–4567, May/Jun. 2024.

[5] J. Liang et al., "Free-space optical (FSO) satellite networks performance analysis: Transmission power, latency, and outage probability," *IEEE Open J. Veh. Technol*., vol. 5, pp. 244–261, 2024.

[6] D. Zhou, M. Sheng, J. Wu, J. Li, and Z. Han, "Gateway placement in integrated satellite-terrestrial networks: Supporting communications and Internet of Remote Things," *IEEE Internet Things J*., vol. 9, no. 6, pp. 4421–4434, Mar. 2022.

[7] R. Kumar and S. Arnon, "SNR optimization for LEO satellite at sub-THz frequencies," *IEEE Trans. Antennas Propag*., vol. 70, no. 6, pp. 4449–4458, Jun. 2022.

[8] P.-H. Chen and R. L.-T. Cho, "The technological trajectory of LEO satellites: Perspectives from main path analysis," *IEEE Trans. Eng. Manag*., vol. 71, pp. 3629–3640, 2024.

[9] L. Sheng, G. Lou, W. Gu, S. Lu, S. Ding, and Z. Ye, "Optimal communication network design of microgrids considering cyber-attacks and time-delays," *IEEE Trans. Smart Grid*, vol. 13, no. 5, pp. 3774–3785, Sep. 2022.

[10] Z. Lian, Y. Zhu, F. Guo, C. Peng, and Q. Zhou, "Distributed cyber resilient control strategy for remote DC microgrids under integrated

Authorized licensed use limited to: HUNAN UNIVERSITY. Downloaded on September 25,2026 at 04:45:13 UTC from IEEE Xplore. Restrictions apply.
© 2026 IEEE. All rights reserved, including rights for text and data mining and training of artificial intelligence and similar technologies. Personal use is permitted, but republication/redistribution requires IEEE permission. See https://www.ieee.org/publications/rights/index.html for more information.

This article has been accepted for publication in IEEE Transactions on Smart Grid. This is the author's version which has not been fully edited and content may change prior to final publication. Citation information: DOI 10.1109/TSG.2026.3715495

satellite terrestrial networks," *IEEE Trans. Ind. Inform.*, vol. 21, no. 3, pp. 2363–2372, Mar. 2025.

[11] X. Lu and J. Lai, "Communication constraints for distributed secondary control of heterogeneous microgrids: A survey," *IEEE Trans. Ind. Appl.*, vol. 57, no. 6, pp. 5636–5648, Nov./Dec. 2021.

[12] S. I. Habibi, M. A. Sheikhi, T. Khalili, S. A. G. K. Abadi, A. Bidram, and J. M. Guerrero, "Multiagent-based nonlinear generalized minimum variance control for islanded AC microgrids," *IEEE Trans. Power Syst.*, vol. 39, no. 1, pp. 316–328, Jan. 2024.

[13] S.-W. Lin, C.-T. Ko, B.-Y. Ye and C.-C. Chu, "Distributed noise-resilient fixed-time consensus secondary control for hybrid inverter-based AC/DC microgrids," *IEEE Trans. Ind. Appl*., vol. 59, no. 6, pp. 7428–7443, Nov./Dec. 2023.

[14] Q. Zhao, R. Chang, Z. Chen and F. Yin, "Diffusion-based distributed multi-frame Kalman filtering with speech distortionless constraint for speech enhancement," *IEEE Trans. Audio, Speech Lang. Process.*, vol. 33, pp. 1063–1077, 2025.

[15] Z. Lian, H. Yu, Y. Chen, M. Shahidehpour, and Q. Zhou, "Secure microgrid clusters under integrated satellite-terrestrial networks: a differential privacy-preserving control strategy," *IEEE Trans. Ind. Electron.*, vol. 73, no. 2, pp. 2104–2115, Feb. 2026.

[16] E. Arcari, A. Iannelli, A. Carron, and M. N. Zeilinger, "Stochastic MPC with robustness to bounded parametric uncertainty," *IEEE Trans. Autom. Control*, vol. 68, no. 12, pp. 7601–7615, Dec. 2023.

[17] T. Yang, H. Li, S. Cai, and Y. Liu, "Distributed voltage control for microgrids against time-varying communication delay interference," *IEEE Trans. Smart Grid*, vol. 15, no. 3, pp. 2410–2423, May 2024.

[18] Y. Yu, G.-P. Liu, and W. Hu, "Coordinated distributed predictive control for voltage regulation of DC microgrids with communication delays and data loss," *IEEE Trans. Smart Grid*, vol. 14, no. 3, pp. 1708–1722, May 2023.

[19] J. Lai, X. Lu, Z. Dong and S. Cheng, "Resilient distributed multiagent control for AC microgrid networks subject to disturbances," *IEEE Trans. Syst. Man Cybern. Syst*., vol. 52, no. 1, pp. 43–53, Jan. 2022.

[20] S. Xing, W. Zheng, F. Deng and C. Chang, "H∞ control for stochastic singular systems with time-varying delays via sampled data controller," *IEEE Trans. Cybern.*, vol. 53, no. 11, pp. 7048–7057, Nov. 2023.

[21] G. Zhao, L. Jin, H. Cui, and Y. Wang, "Distributed dynamic event-triggered secondary control for islanded microgrids with disturbances and communication delays: A hybrid systems approach," *IEEE Trans. Ind. Inform*., vol. 19, no. 8, pp. 8795–8805, Aug. 2023.

[22] Z. Xia, Q. Zhou, M. Shahidehpour, and Z. Shuai, "Cognitive radio empowered smart grid," *IEEE Trans. Smart Grid*, vol. 17, no. 3, pp. 2582–2598, May 2026.

[23] Z. Zhang, Y. Wu, Z. Ma, X. Lei, L. Lei, and Z. Wei, "Coordinated multi-satellite transmission for OTFS-Based 6G LEO satellite communication systems," *IEEE J. Sel. Areas Commun.*, vol. 43, no. 1, pp. 156–170, Jan. 2025.

[24] X. Zhu and C. Jiang, "Delay optimization for cooperative multi-tier computing in integrated satellite-terrestrial networks," *IEEE J. Sel. Areas Commun.*, vol. 41, no. 2, pp. 366–380, Feb. 2023.

[25] S. Abhinav, I. D. Schizas, F. L. Lewis, and A. Davoudi, "Distributed noise-resilient networked synchrony of active distribution systems," *IEEE Trans. Smart Grid*, vol. 9, no. 2, pp. 836–846, Mar. 2018.

[26] Y. Lyu, H. Hu, R. Fan, Z. Liu, J. An, and S. Mao, "Dynamic routing for integrated satellite-terrestrial networks: A constrained multi-agent reinforcement learning approach," *IEEE J. Sel. Areas Commun.*, vol. 42, no. 5, pp. 1204–1218, May 2024.

[27] Q. Yang, D. I. Laurenson, and J. A. Barria, "On the use of LEO satellite constellation for active network management in power distribution networks," *IEEE Trans. Smart Grid*, vol. 3, no. 3, pp. 1371–1381, Sep. 2012.

[28] K. Zhang, B. Jiang, and P. Shi, "Adjustable parameter-based distributed fault estimation observer design for multiagent systems with directed graphs," *IEEE Trans. Cybern*., vol. 47, no. 2, pp. 306–314, Feb. 2017.

Authorized licensed use limited to: HUNAN UNIVERSITY. Downloaded on September 25,2026 at 04:45:13 UTC from IEEE Xplore. Restrictions apply.
© 2026 IEEE. All rights reserved, including rights for text and data mining and training of artificial intelligence and similar technologies. Personal use is permitted, but republication/redistribution requires IEEE permission. See https://www.ieee.org/publications/rights/index.html for more information.